Vibrational properties of crystalline Sb_2Te_3 from first principles

2009 J. Phys.: Condens. Matter 21 095410

(http://iopscience.iop.org/0953-8984/21/9/095410)

J. Phys.: Condens. Matter **21** (2009) 095410 (6pp) doi:10.1088/0953-8984/21/9/095410

Vibrational properties of crystalline Sb_2Te_3 from first principles

G C Sosso[1], S Caravati[1,2] and M Bernasconi[1]

[1] Dipartimento di Scienza dei Materiali, Università di Milano-Bicocca, Via R Cozzi 53, I-20125 Milano, Italy
[2] Department of Chemistry and Applied Biosciences, ETH Zurich, USI Campus, Via Giuseppe Buffi 13, CH-6900 Lugano, Switzerland

Received 29 November 2008, in final form 13 January 2009
Published 4 February 2009
Online at stacks.iop.org/JPhysCM/21/095410

Abstract
Phonon dispersion relations and infrared and Raman spectra of crystalline Sb_2Te_3 were computed within density functional perturbation theory. Overall good agreement with experiments is obtained, which allows us to assign the Raman and IR peaks to specific phonons.

(Some figures in this article are in colour only in the electronic version)

S Supplementary data are available from stacks.iop.org/JPhysCM/21/095410

1. Introduction

Sb_2Te_3 is a material of interest for applications in thermoelectric devices [1]. It is also a component of chalcogenide alloys exploited as phase change materials in information storage devices [2]. In this work, we investigate the vibrational properties of crystalline Sb_2Te_3 from first principles aimed at assigning the peaks of the experimental Raman and IR spectra and at reproducing experimental phonon dispersion relations. The calculations assess the reliability of a framework based on density functional theory (DFT) in reproducing the vibrational spectrum of Sb_2Te_3 of relevance for future *ab initio* investigation of its thermoelectric properties. The results also aid future analysis of the vibrational spectra of the ternary GeSbTe alloys of great technological relevance for information storage, such as $(GeTe)_2(Sb_2Te_3)$ [2, 3] which crystallizes in a hexagonal phase similar in structure to Sb_2Te_3.

2. Computational details

Calculations were performed within the framework of DFT with exchange and correlation energy functional in the generalized gradient approximation (GGA) of Perdew–Burke–Ernzerhof (PBE [4]) and norm-conserving pseudopotentials as implemented in the codes PWSCF and PHONONS [5]. Only outermost s and p electrons were considered in the valence. For Te we also considered including semicore d states in the valence as discussed in section 3. Kohn–Sham (KS) orbitals were expanded in a plane wave basis up to a kinetic cutoff of 20 Ryd. Brillouin zone (BZ) integration was performed over a $6 \times 6 \times 6$ Monkhorst–Pack (MP) mesh [6]. Equilibrium geometries have been obtained by optimizing internal structure and lattice parameters. Residual anisotropy in the stress tensor at the optimized lattice parameter at each volume is below 0.3 kbar. The energy versus volume data were fitted to a Murnaghan function [7]. Infrared and Raman spectra were obtained from effective charges, dielectric susceptibilities and phonons at the Γ point within density functional perturbation theory [8]. Relevant formulae for the calculation of the IR and Raman spectra are given in section 3. Phonon dispersion relations were computed along the symmetry direction for which inelastic neutron scattering data are available [9].

3. Results

3.1. Structural and electronic properties

Crystalline Sb_2Te_3 has a rhombohedral geometry ($R\bar{3}m$ space group (D^5_{3d})) with five atoms per unit cell [10]. The crystal structure can be better visualized in the conventional hexagonal supercell with three formula units (figure 1). In the hexagonal cell we recognize three slabs, each formed by five hexagonal layers stacked along c in the sequence Te–Sb–Te–Sb–Te, each layer containing a single atom in the unit cell. The weak Te–Te bonds, 3.736 Å long [10], connecting adjacent slabs are not shown in figure 1 to emphasize the presence of Sb_2Te_3 structural units. The three atoms independent by symmetry are at crystallographic positions Te1 $= (0, 0, 0)$, Te2 $= (0, 0, x)$ and Sb $= (0, 0, y)$ (figure 1).

The calculated parameters x and y, bond lengths and lattice parameters at equilibrium are compared in table 1 with

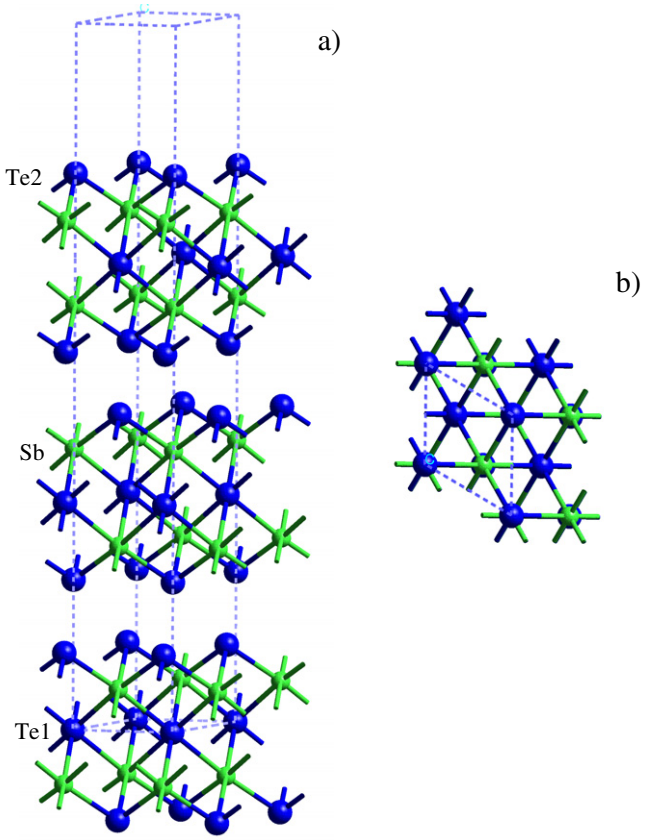

Figure 1. Structure of Sb_2Te_3 in the conventional hexagonal supercell (three formula units). (a) Side view. (b) Top view along the hexagonal *c* axis. The three atoms independent by symmetry are labeled.

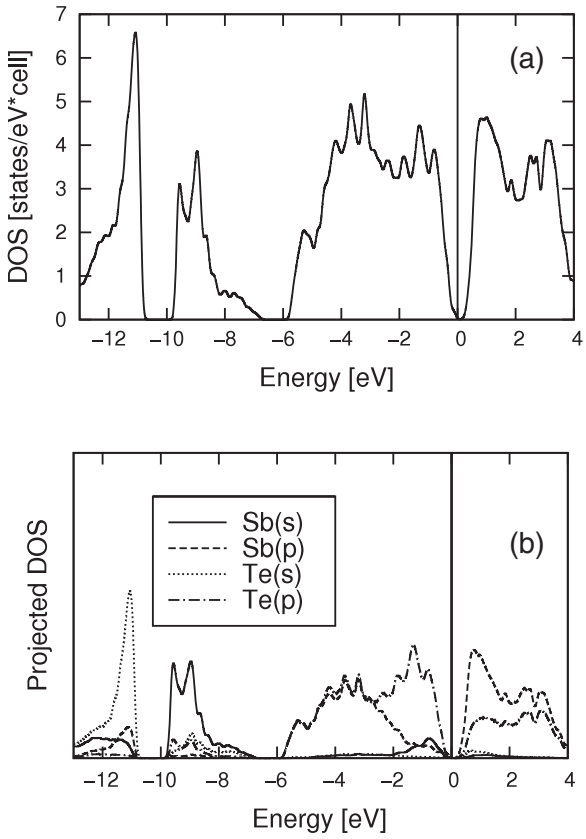

Figure 2. Electronic density of states (DOS) of Sb_2Te_3 calculated on a $20 \times 20 \times 20$ mesh in the irreducible Brillouin zone. Each electronic level is broadening with a Gaussian function 0.09 eV wide. (a) Total DOS. (b) DOS projected on s and p orbitals of Te and Sb atoms. The zero of energy is the top of the valence band.

Table 1. Theoretical and experimental lattice parameters, *a* and *c* (Å), of the conventional hexagonal cell, parameters *x* and *y* which assign the position of atoms independent by symmetry, Te2 = (0, 0, *x*) and Sb = (0, 0, *y*), in crystallographic units and bond lengths (Å). Experimental data are from [10]. Previous theoretical PBE results from [11] and [12].

	This work	This work (exp. cell)	Theory[a] [11]	Theory[b] [12]	Exp. [10]
a	4.316		4.35	4.44	4.264
c	31.037		30.844	30.29	30.458
x	0.785	0.788	0.7864	0.791	0.7872
y	0.397	0.398	0.3977	0.400	0.3988
Te1–Sb	3.178	3.156	3.201	3.263	3.168
Sb–Te2	3.020	3.005	3.037	3.102	2.979
Te2–Te2′	3.891	3.695	3.833	3.626	3.736

[a] Pseudopotential, plane wave calculation [11].

[b] All-electron, full potential, linearized augmented plane wave calculation [12].

experimental data [10] and previous theoretical works [11, 12]. Theoretical bond lengths are reported both at the theoretical and at the experimental equilibrium lattice parameters. The calculated bulk modulus is 22 GPa.

The agreement with experimental data is overall acceptable, but for a misfit in the Te–Te bond length which is much larger than the usual errors within DFT-GGA. The bond lengths are brought to a better agreement with experiments by fixing the lattice parameters to the experimental values. The inclusion of semicore d states of Te does not lead to improvements in the theoretical equilibrium geometry, the structural parameters of table 1 turning out to be $a = 4.338$ Å, $c = 31.338$ Å, $x = 0.785$, $y = 0.397$, d(Te1–Sb) = 3.196 Å, d(Sb–Te2) = 3.033 Å and d(Te2–Te2′) = 3.949 Å. This misfit can be ascribed to deficiencies of most common DFT-GGA functionals in describing weak bonds such as the Te–Te bond in this system.

The calculated electronic density of states of Sb_2Te_3 at the theoretical equilibrium volume is reported in figure 2. The system is insulating, with a small direct bandgap at the Γ point of 0.15 eV. Inclusion of the spin–orbit interaction, here neglected, changes several details of the band structure, causing the bandgap to become indirect and to widen to 0.278 eV [11] (experimental value 0.28 [13]).

3.2. Vibrational properties

Phonons at the Γ point are classified according to the irreducible representations of the point group D_{3d} as

$$\Gamma = 2(A_{1g} + E_g) + 3(E_u + A_{2u}). \quad (1)$$

One E_u and one A_{2u} are acoustic modes. The modes which display a dipole moment (u-modes) couple to the inner

Table 2. Frequency (cm^{-1}) and character of Γ-point phonons of the optimized geometry at the theoretical and experimental (exp. cell) equilibrium lattice parameters. The g-modes (Raman active) and u-modes (IR-active) are reported separately. Acoustic modes (at zero frequency) are omitted. For g-modes the coefficients of the Raman tensor (equation (8) and matrices (9)) are reported in units of 10^{-4} Å^3. For u-modes, two sets of frequencies are reported. Frequencies in parentheses are obtained by including the contributions of the non-analytical part of the dynamical matrix with $\vec{q}$ parallel to the hexagonal axes c or a (equation (2)) for A_{2u} or E_u modes, respectively. The dipole moment **p** (equation (5), in atomic units) of u-modes is also given.

Mode	This work	This work (exp. cell)	Exp.[a]	a^2 or c^2	b^2 or d^2
E_g (1)	46	49		0.00	0.18
A_{1g} (1)	62	67	69	2.97	4.35
E_g (2)	113	117	112	12.85	10.12
A_{1g} (2)	166	169	165	3.28	0.46

Mode	This work	This work (exp. cell)	Exp.[a]	p_x	p_y	p_z
E_u (2)	72	77 (128)	67	0.0214	0.0152	0.0000
E_u (3)	99	100 (100)		0.0005	0.0009	0.0000
A_{2u} (2)	108	109 (114)		0.0000	0.0000	0.0053
A_{2u} (3)	145	146 (154)		0.0000	0.0000	0.0046

[a] Experimental data are from Raman and IR spectra of [14]. A_{2u} (1) and E_u (1) are acoustic modes.

macroscopic longitudinal electric field which shifts the LO phonon frequencies via the non-analytical contribution to the dynamical matrix

$$D^{\mathrm{NA}}_{\alpha\beta}(\kappa,\kappa') = \frac{4\pi}{V_o}\frac{\sum_{\alpha'\beta'} Z_{\alpha\alpha'}(\kappa) q_{\alpha'} Z_{\beta\beta'}(\kappa') q_{\beta'}}{\mathbf{q}\cdot\underline{\underline{\epsilon}}^{\infty}\cdot\mathbf{q}}, \qquad (2)$$

where $\underline{\underline{Z}}$ and $\underline{\underline{\epsilon}}^{\infty}$ are the effective charges and electronic dielectric tensors, V_o is the unit cell volume and **q** is the phonon wavevector. The macroscopic field contribution to the dynamical matrix introduces an angular dispersion of the phonons at the Γ point, i.e. the limit of the phonon bands $\omega(\mathbf{q})$ for $\mathbf{q} \to 0$ depends on the angle formed by **q** with the optical axis. The calculated dielectric tensor $\underline{\underline{\epsilon}}^{\infty}$ and the effective charges $\underline{\underline{Z}}$ for the optimized geometry at the experimental lattice parameters are given below in Cartesian coordinates:

$$\underline{\underline{\epsilon}}^{\infty} = \begin{bmatrix} 64.4 & \cdot & \cdot \\ \cdot & 64.4 & \cdot \\ \cdot & \cdot & 47.8 \end{bmatrix}$$

$$\underline{\underline{Z}}(\mathrm{Te1}) = \begin{bmatrix} -6.7 & \cdot & \cdot \\ \cdot & -6.7 & \cdot \\ \cdot & \cdot & -5.4 \end{bmatrix} \qquad (3)$$

$$\underline{\underline{Z}}(\mathrm{Te2}) = \begin{bmatrix} -5.5 & \cdot & \cdot \\ \cdot & -5.5 & \cdot \\ \cdot & \cdot & -1.2 \end{bmatrix}$$

$$\underline{\underline{Z}}(\mathrm{Sb}) = \begin{bmatrix} 9.1 & \cdot & \cdot \\ \cdot & 9.1 & \cdot \\ \cdot & \cdot & 4.0 \end{bmatrix}.$$

The available experimental dielectric constant is $\epsilon^{\infty}_{xx} = 51$ [14]. The calculated phonon frequencies at the Γ point are reported in table 2 for the optimized geometry both at the theoretical and equilibrium lattice parameters. Two sets of frequencies are reported, namely those obtained by neglecting the macroscopic field and those obtained by including the contribution of the non-analytical part of the dynamical matrix with **q** parallel to the c or a axes (equation (2)) for modes A_{2u} or E_u, respectively. The displacement patterns of all the modes are sketched in figure 3 and are available in a MOLDEN file as additional material (available from stacks.iop.org/JPhysCM/21/095410).

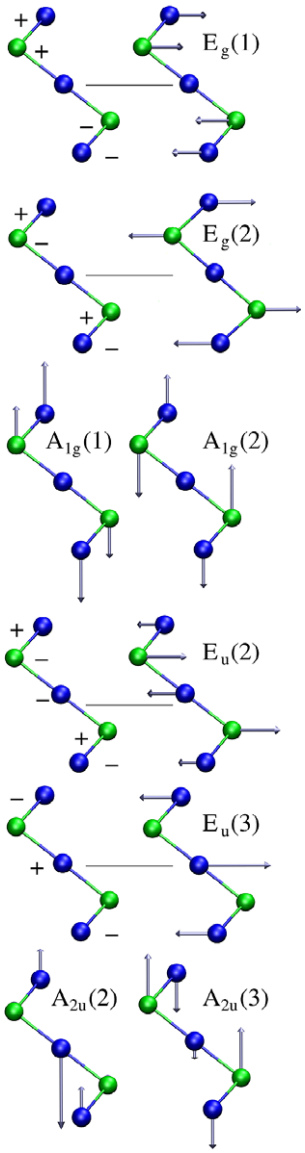

Figure 3. Sketch of the displacement patterns of phonons at the Γ point. E and A modes involve displacements in the a–b plane and along the c axis.

The dielectric function, which controls the IR absorption, is given in terms of phonons and effective charges by

$$\underline{\underline{\epsilon}}(\omega) = \underline{\underline{\epsilon}}^{\infty} + \frac{4\pi}{V_o}\sum_{j=1}^{3N} p_\alpha(j)\, p_\beta(j)\frac{2\omega_j}{\omega_j^2 - \omega^2} \qquad (4)$$

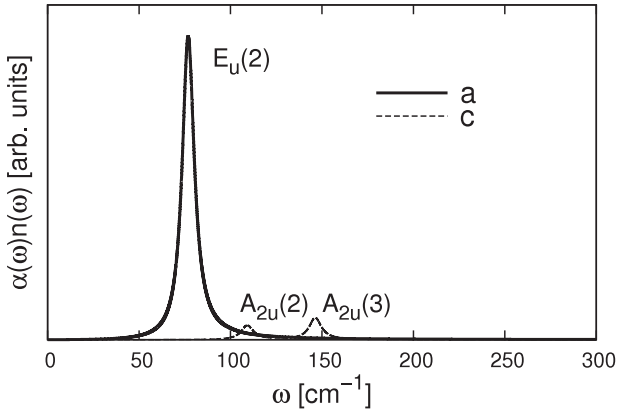

Figure 4. IR spectra $\alpha(\omega)n(\omega)$ (see text) for light polarized along the principal axes a and c of the hexagonal crystal.

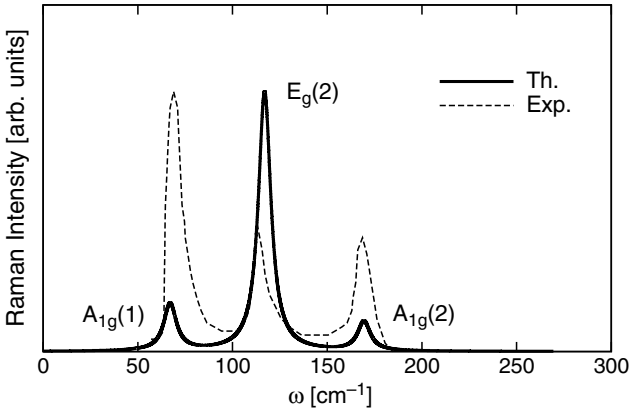

Figure 5. Experimental (dashed line, adapted from [14]) and theoretical (continuous lines) Raman spectra for crystalline Sb_2Te_3 in backscattering geometry for non-polarized light impinging on a single crystal along the c axis of the hexagonal cell. The labeling of the modes is the same as in table 2, while the corresponding displacement patterns are sketched in figure 3. The δ functions in equation (7) are approximated by Lorentzian functions with a constant width of 4 cm^{-1}.

where $\mathbf{p}(j)$ is defined by

$$\mathbf{p}(j) = \sum_{\kappa=1}^{N} \underline{\underline{Z}}(\kappa) \frac{\mathbf{e}(j,\kappa)}{\sqrt{2M_\kappa \omega_j}} \tag{5}$$

and is reported for all u-modes in table 2. The sum over κ runs over the N atoms in the unit cell with masses M_κ, and $\mathbf{e}(j,\kappa)$ and ω_j are the eigenstates and the eigenvalues of the dynamical matrix at the Γ point, without the contribution of the macroscopic field. The dielectric function in equation (4) allows computing the IR absorption for a generic polarization of the transmitted light by solving the Fresnel equation [15]. For the particular case of light linearly polarized with an electric field along the principal axis, the absorption coefficient has the simple form

$$\begin{aligned} \alpha_i(\omega) &= \frac{\omega}{n_i(\omega)c} \mathrm{Im}\, \epsilon_{ii}(\omega + i\eta, \eta \to 0) \\ &= \frac{4\pi^2}{V_o n_i(\omega) c} \sum_j \omega_j \, |p_i(j)|^2 \, \delta(\omega - \omega_j) \end{aligned} \tag{6}$$

where i is the crystallographic direction of the hexagonal cell (a or c), c is the velocity of light in vacuum and $n_i(\omega)$ is the (frequency-dependent) real part of the refractive index. The calculated IR absorption spectra $\alpha_i(\omega)n_i(\omega)$ are shown in figure 4. The δ functions in equation (6) are approximated by Lorentzian functions with a constant width of 4 cm^{-1}. The experimental IR spectrum [14] for a single crystal revealed only an E_u mode at 67 cm^{-1}, in good agreement with the position of the main E_u mode and the weakness of the other structures in the theoretical IR spectra in figure 4.

The differential cross section for Raman scattering (Stokes) in non-resonant conditions is given by the following expression (for a unit volume of scattering sample):

$$\frac{\mathrm{d}^2\sigma}{\mathrm{d}\Omega \, \mathrm{d}\omega} = \sum_j \frac{\omega_S^4}{c^4} |\mathbf{e}_S \cdot \underline{\underline{R}}^j \cdot \mathbf{e}_L|^2 (n_B(\omega) + 1) \delta(\omega - \omega_j), \tag{7}$$

where $n_B(\omega)$ is the Bose factor, ω_S is the frequency of the scattered light, and $\mathbf{e}_S$ and $\mathbf{e}_L$ are the polarization vectors of the scattered and incident light, respectively. The Raman tensor $\underline{\underline{R}}^j$ associated with the jth phonon is given by

$$R^j_{\alpha\beta} = \sqrt{\frac{V_o \hbar}{2\omega_j}} \sum_{\kappa=1}^{N} \frac{\partial \chi^\infty_{\alpha\beta}}{\partial \mathbf{r}(\kappa)} \cdot \frac{\mathbf{e}(j,\kappa)}{\sqrt{M_\kappa}}, \tag{8}$$

where V_o is the unit cell volume, $\mathbf{r}(\kappa)$ is the position of the κth atom and $\underline{\underline{\chi}}^\infty = (\underline{\underline{\varepsilon}}^\infty - \mathbf{1})/4\pi$ is the electronic susceptibility. The tensors $\underline{\underline{R}}^j$ were computed from $\underline{\underline{\chi}}^\infty$ by finite differences, moving the atoms independent by symmetry with a maximum displacement of 0.01 Å. The Raman tensor (equation (8)) for the Raman-active irreducible representations (all the g-modes) has the following form [16]:

$$\mathrm{A_{1g}} \Rightarrow \begin{bmatrix} a & \cdot & \cdot \\ \cdot & a & \cdot \\ \cdot & \cdot & b \end{bmatrix}$$

$$\mathrm{E_g}(x) \Rightarrow \begin{bmatrix} c & \cdot & \cdot \\ \cdot & -c & d \\ \cdot & d & \cdot \end{bmatrix} \qquad \mathrm{E_g}(y) \Rightarrow \begin{bmatrix} \cdot & -c & -d \\ -c & \cdot & \cdot \\ -d & \cdot & \cdot \end{bmatrix}. \tag{9}$$

The coefficients of the Raman tensor (in equation (9)), calculated from first principles as outlined above, are reported in table 2 for the optimized geometry at the experimental lattice parameters. The experimental Raman spectrum [14] is available in backscattering geometry for non-polarized light impinging on a single crystal along the c axis of the hexagonal cell. In this geometry one selects the coefficients a and c of the Raman tensor of modes A_{1g} and E_g, respectively. Theoretical (for the optimized geometry at the experimental lattice parameters) and experimental Raman spectra at the experimental set-up geometry are compared in figure 5. They are in good agreement for the peak positions, but one observes large discrepancies in the relative peak intensities.

However, one must note that the experimental spectrum is recorded with a laser wavelength of 1.9 eV, well above the

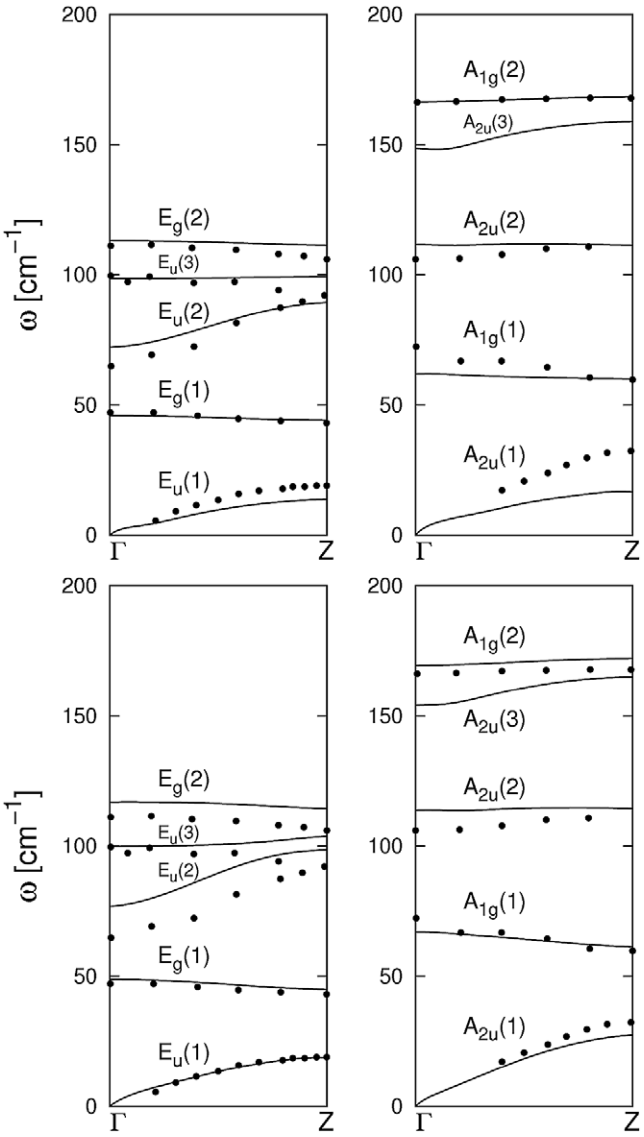

Figure 6. Phonon dispersion relations along the Γ–Z direction (along the *c* axis). Dots correspond to experimental inelastic neutron scattering data of [9]. Branches corresponding to A and E zone-center phonons are reported in separate panels. The upper and lower panels correspond to the optimized geometry at the theoretical and experimental equilibrium lattice parameters, respectively.

electronic bandgap of Sb_2Te_3. Effects of electronic resonances, not included in the off-resonance formula of equation (7), might strongly affect the Raman intensities of different peaks and account for the misfit between theory and experiments.

Phonon dispersion relations were computed only along the Γ–Z direction for which inelastic neutron scattering data are available [9]. The dynamical matrices were computed within density functional perturbation theory [8] for 20 **q**-points along the Γ–Z path for the optimized geometries at both the theoretical and experimental equilibrium lattice parameters. The resulting phonon curves are compared with inelastic neutron scattering data in figure 6. Phonons at the Γ and Z points were also computed with semicore d states of Te in the valence for the optimized geometry at the experimental lattice parameters. The resulting frequencies differ by less than 2 cm^{-1} from the corresponding theoretical data in figure 2 for which the d states of Te are frozen in the core.

The agreement with experimental data on the phonon dispersion relations is overall good considering the misfit in the Te–Te bond lengths at the theoretical equilibrium geometry mentioned above. The comparison between the experimental data and the calculated phonon frequencies at the theoretical and experimental equilibrium lattice parameters shows that the length of the weak Te–Te bond affects only slightly the optical branches while it is crucial to reproduce the longitudinal acoustic branch along the Γ–Z direction.

4. Conclusions

Based on density functional perturbation theory we calculated Raman and IR spectra and phonon dispersion relations of crystalline Sb_2Te_3. The overall agreement with experimental data is fair but there is room for improvement. Overestimation of the Te–Te interplanar bond length results in a sizable underestimation of the frequencies of zone boundary acoustic longitudinal phonons which are precisely modulated by the interlayer distance. Thus, it is worth pursuing further work by exploring, for instance, recently developed exchange and correlation functionals (e.g. the approximation of Tao *et al* [17]) which might perform better than the most commonly used PBE functional in the presence of relatively weak bonds such as the Te–Te interplanar bond in Sb_2Te_3.

Acknowledgments

The author gratefully acknowledges the computer resources, technical expertise and assistance provided by the Barcelona Supercomputing Center—Centro Nacional de Supercomputación, by the DEISA Consortium under project PHASE-MAT, and by CSCS (Manno, CH).

References

[1] Snyder G J and Tobere E S 2008 *Nat. Mater.* **7** 105
[2] Wuttig M and Yamada M 2007 *Nat. Mater.* **6** 824
[3] Caravati S, Bernasconi M, Kühne T D, Krack M and Parrinello M 2007 *Appl. Phys. Lett.* **91** 171906
[4] Perdew J P, Burke K and Ernzerhof M 1996 *Phys. Rev. Lett.* **77** 3865
[5] Baroni S, De Gironcoli S, Dal Corso A and Giannozzi P http://www.pwscf.org
[6] Monkhorst H J and Pack J D 1976 *Phys. Rev.* B **13** 5188
[7] Murnaghan D 1944 *Proc. Natl Acad. Sci. USA* **30** 224
[8] Baroni S, De Gironcoli S, Dal Corso A and Giannozzi P 2001 *Rev. Mod. Phys.* **73** 515
[9] Landolt–Börnstein 1983 Antimony telluride (Sb_2Te_3) phonon dispersion, phonon frequencies *Numerical Data and Functional Relationships in Science and Technology (New Series, Group III (Condensed Matter),* vol 41 *(Semiconductors),* subvolume C *(Non Tetrahedrally Bonded Elements and Binary Compounds I)*) ed O Madelung, M Schulz and H Weiss (New York: Springer) doi:10.1007/10681727_1054
[10] Anderson T L and Krause H B 1974 *Acta Crystallogr.* B **30** 1307

[11] Thonhauser T, Scheidemantel T J, Sofo J O, Badding J V and Mahan G D 2003 *Phys. Rev.* B **68** 085201
[12] Wang G and Cagin T 2007 *Phys. Rev.* B **76** 075201
[13] Landolt–Börnstein 1983 Antimony telluride (Sb_2Te_3) band structure, energy gap *Numerical Data and Functional Relationships in Science and Technology* (*New Series, Group III (Condensed Matter),* vol 41 *(Semiconductors),* subvolume C *(Non Tetrahedrally Bonded Elements and Binary Compounds I)*) ed O Madelung, M Schulz and H Weiss (New York: Springer) doi:10.1007/10681727_1043
[14] Richter W, Köhler H and Becker C R 1977 *Phys. Status Solidi* b **84** 619
[15] Claus R 1980 *Phys. Status Solidi* b **100** 9
[16] Loudon R 2001 *Adv. Phys.* **50** 813
[17] Tao J, Perdew J P, Staroverov V N and Scuseria G E 2003 *Phys. Rev. Lett.* **91** 146401